

PAPI-Reg: Patch-to-Pixel Solution for Efficient Cross-Modal Registration between LiDAR Point Cloud and Camera Image

Yuanchao Yue, Zhengxin Li, Wei Zhang, Huiyuan*

Key Laboratory of Machine Intelligence and System Control, Ministry of Education

School of Control Science and Engineering, Shandong University

202234945@sdu.edu.cn, lizx@mail.sdu.edu.cn, davidzhang@sdu.edu.cn, huiyuan@sdu.edu.cn

Abstract

The primary requirement for cross-modal data fusion is the precise alignment of data from different sensors. However, the calibration between LiDAR point clouds and camera images is typically time-consuming and needs external calibration board or specific environmental features. Cross-modal registration effectively solves this problem by aligning the data directly without requiring external calibration. However, due to the domain gap between the point cloud and the image, existing methods rarely achieve satisfactory registration accuracy while maintaining real-time performance. To address this issue, we propose a framework that projects point clouds into several 2D representations for matching with camera images, which not only leverages the geometric characteristic of LiDAR point clouds more effectively but also bridge the domain gap between the point cloud and image. Moreover, to tackle the challenges of cross modal differences and the limited overlap between LiDAR point clouds and images in the image matching task, we introduce a multi-scale feature extraction network to effectively extract features from both camera images and the projection maps of LiDAR point cloud. Additionally, we propose a patch-to-pixel matching network to provide more effective supervision and achieve higher accuracy. We validate the performance of our model through experiments on the KITTI and nuScenes datasets. Our network achieves real-time performance and extremely high registration accuracy. On the KITTI dataset, our model achieves a registration accuracy rate of over 99%.

1. Introduction

In autonomous driving and robot systems, the fusion between data collected from different sensors now plays an important role in many downstream tasks, such as object detection [1, 6, 15] and segmentation [5, 31, 33]. We can

achieve better accuracy and efficiency by using these fused data, thereby ensuring safety and robustness in complex environments. Among these methods, the most common process is to perform a fusion of the LiDAR (solid-state LiDAR or rotating LiDAR, etc.) point cloud and the camera (high-definition cameras or infrared cameras, etc.) image.

However, the primary condition of a successful fusion is an accurate alignment between these data. A commonly used method to deal with the alignment task between sensors is to calculate the external parameters between sensors using a checkerboard [14], which we call off-line calibration. We can make a high-accuracy alignment between sensors by using these types of methods and unavoidable time costs. In addition, some online calibration methods [13, 27, 36] are proposed to correct external parameter errors caused by bumps or vibrations. These online calibration methods can modify the deviations within a limited error range. However, they will lose effectiveness when the errors are too large. Although these methods can achieve high-accuracy alignment, these complicated calibration processes make data fusion preprocessing time-consuming and inefficient. Whenever the deployment of sensors has changed, these processes have to be repeated.

Why not propose a method to bypass these calibration processes and save manpower and resources by directly doing a registration between the collected data? Cross-modal registration methods have emerged to address this challenge. Recent cross-modal registration methods [9, 21] can solve this cross-modal data alignment task by using specific deep learning networks. However, the cross-modal registration process typically involves comparing the similarity of the high-dimensional features between point clouds and images to establish correspondences, and the domain gap between 3D and 2D data always influence this process, as we showed in Fig. 1. Specifically, there is a dimensional and informational difference between the 3D spatial data of the point cloud and the 2D texture information of the image. Although some existing methods attempt to decline these influence by exchanging feature information [24] or

*Corresponding author. huiyuan@sdu.edu.cn

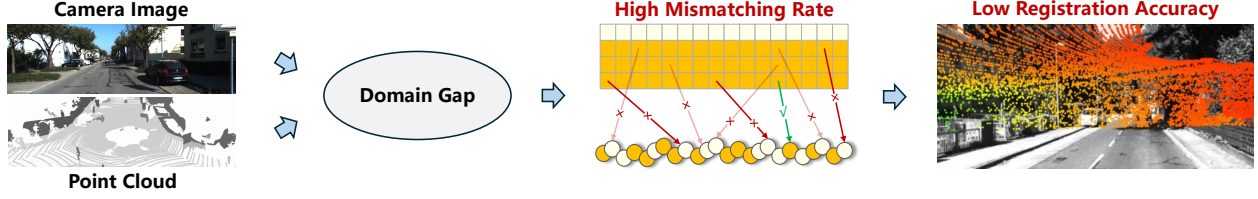


Figure 1. The problem about the domain gap in the cross-modal registration task. Due to the dimensional differences between point clouds and images, the matching failure rate between them is high, which in turn reduces the registration accuracy.

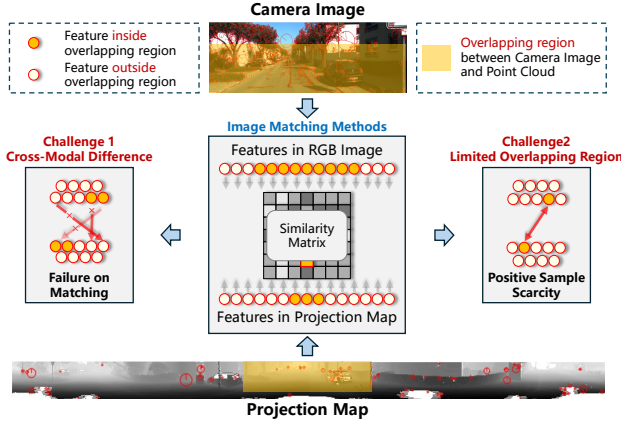


Figure 2. The challenge we faced in the matching task between projection map and camera image. The cross-modal difference between the camera image and the projection map will make it difficult to the feature matching. Additionally, the scarcity of positive samples caused by the limited overlapping region will lead to the network’s supervision problem.

using feature extraction networks with more similar structures [39], this domain gap still affect the accuracy of the registration, especially leading to a high mismatching rate.

Besides, the commonly used point cloud feature extraction network in the cross-modal registration task (e.g., PointNet++ [23], sparse convolution network[7]) always treats the LiDAR point cloud simply as a series of unordered points or voxels, which fails to effectively use the spatial and geometric characteristics of the point cloud. Therefore, to make better use of the scanning characteristics of LiDAR to bridge the domain gap, we introduce a method to project point clouds into 2D representations: a range map and a reflectance map. Although using these projection methods is not new in other downstream tasks involving LiDAR point clouds, they have not been fully leveraged in cross-modal registration methods. Moreover, mapping point clouds to pixels in 2D representations offers a data format that implicitly contains more geometric information, making it more effective and accurate than using unordered sparse point clouds. This projection approach will enable more effective feature extraction and bridge the domain gap difference between point clouds and images. Furthermore, we com-

bined the use of the two projection maps containing different types of information to enhance the system’s robustness for registration across various scenarios.

After the projection, we transform the cross-modal registration task to an image registration task between the camera image and the projection maps. Common image registration methods are generally accomplished through key point matching. Due to the cross-modal differences between the projected 2D map and the camera image, traditional key point registration methods cannot be directly applied to this task, as we showed in Fig. 2. Furthermore, the overlapping region between the 2D map and the camera image is often limited in practical scenarios, therefore the proportion of truly matched point pairs becomes extremely small, leading to positive pair scarcity. For existing deep learning-based image matching methods, this scarcity can cause supervision difficulties, making the network hard to converge and increasing the number of outliers, which in turn raises the likelihood of registration failures.

To address these challenges, we designed a multi-scale feature extraction network to mitigate the cross-modal differences between images and projection maps, effectively extracting features. Additionally, we introduced a patch-to-pixel feature matching framework. Specifically, patch-level searching addresses the supervision and success rate issues caused by positive sample scarcity, while pixel-level matching enhances registration accuracy. Our experiment part has proved that our network design achieves high accuracy while maintaining low computational complexity. In conclusion, our contributions are as follows.

1. We propose a robust registration framework that leverages range map and reflectance map features for cross-modal registration between LiDAR point clouds and camera images, which can achieve a registration accuracy rate of over 99% in the KITTI dataset.
2. To address the cross-modal differences between the projection maps and the camera images in the current task, we propose a multi-scale feature extraction network that efficiently extracts features from both the images and the two different types of projection maps simultaneously.
3. We introduce a patch-to-pixel feature matching framework, which not only resolves the supervision problems that arise from the limited overlap between the projec-

tion map and the camera image but also enhances registration accuracy.

2. Related Work

2.1. Off-line Calibration Methods

Traditional offline extrinsic calibration methods [14, 40] are typically conducted before system operation, using manually placed prominent markers to identify 2D-3D correspondences and then estimate the external parameters between sensors using the least-square method [38]. These markers, such as checkerboard, generally contain distinct features on points [12], lines [2], or planes [37]. After establishing the correspondence between 2D and 3D feature points [29]. Such methods are performed before system deployment and can achieve high calibration accuracy. However, the marker placement and calibration process often require significant manpower and resources. If the sensor system’s relative poses are actively changed or vibrations or shocks during operation cause sensor position shifts, the calibration needs to be repeated, which is time-consuming and labor-intensive.

2.2. Online Calibration Methods

Subsequently, many online calibration methods were proposed to optimize minor errors that occur during system operation, such as those caused by vibrations, after initial offline calibration. Existing approaches include using MLPs to estimate deviations [13, 19, 36], keypoint-based methods[35], and techniques that leverage objects [28] or segmentation [32, 42]. These real-time optimization techniques improve data alignment and enhance data fusion, leading to better performance in downstream tasks. However, these methods rely on the initial extrinsic parameters obtained from prior calibration and lose effectiveness when there are significant deviations between the actual and initial parameters. Moreover, deploying online calibration on top of complex offline calibration processes further increases costs.

2.3. Cross-modal registration Methods

Cross-modal registration methods are often used in visual localization tasks [3, 25, 41], where the goal is to estimate the camera extrinsic parameters in the world coordinate system defined by large-scale point clouds. Traditionally, these methods are based on 2D visual descriptors [8, 26] to achieve alignment. Later advancements have introduced cross-dimensional descriptors [9, 21, 30] designed for direct cross-modal matching. These methods generally involve extracting features from different modalities to create high-dimensional representations, using feature similarity in this space to establish correspondences. Subsequently, transformation matrices are estimated using techniques like

EPnP [16].

For matching LiDAR point clouds and images, approaches like DeepI2P [17] reformulates the matching task into a classification problem to tackle cross-modal challenges. CorrI2P [24] later improves registration performance by leveraging overlap region extraction and feature exchange modules. VP2P-Match [39] identifies the inherent differences between MLP networks [22] used for point cloud feature extraction and CNNs used for image processing. By employing voxel sparse convolution, it reduced feature discrepancies and achieved better performance. However, these methods often treat point clouds as unordered sets of points or voxels, failing to fully use the geometric characteristics of LiDAR point clouds.

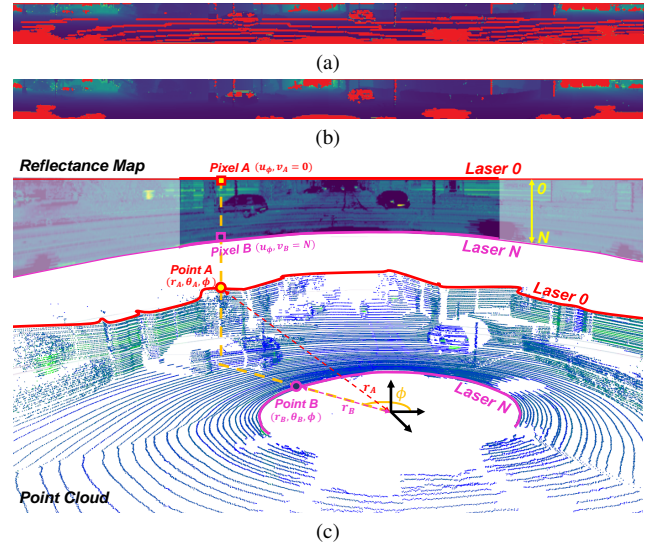


Figure 3. Visualizations of the projection map, (a) Projected map by spherical projection. The red area represents the empty holes. (b) Projected map from modified projection method using LaserID. The red area represents the empty holes. (c) The detailed process of modified projection method using LaserID.

3. Proposed Method

3.1. Problem Statement

Given an RGB image $\mathbf{I}_C \in \mathbb{N}^{H \times W \times 3}$ and a point cloud $\mathbf{P}_L \in \mathbb{R}^{N \times 4}$, where the four dimensions of the point cloud represent the spatial coordinates (x, y, z) and the reflectance intensity r , respectively, our goal is to estimate the rigid transformation matrix \mathbf{T} to align the 3D points to the 2D image coordinates. Matrix \mathbf{T} is given by a translation vector $\mathbf{t} \in \mathbb{R}^3$ and a rotation matrix $\mathbf{R} \in \text{SO}(3)$ as follow:

$$\mathbf{T} = \begin{bmatrix} \mathbf{R} & \mathbf{t} \\ \mathbf{0} & 1 \end{bmatrix} \in \text{SE}(3). \quad (1)$$

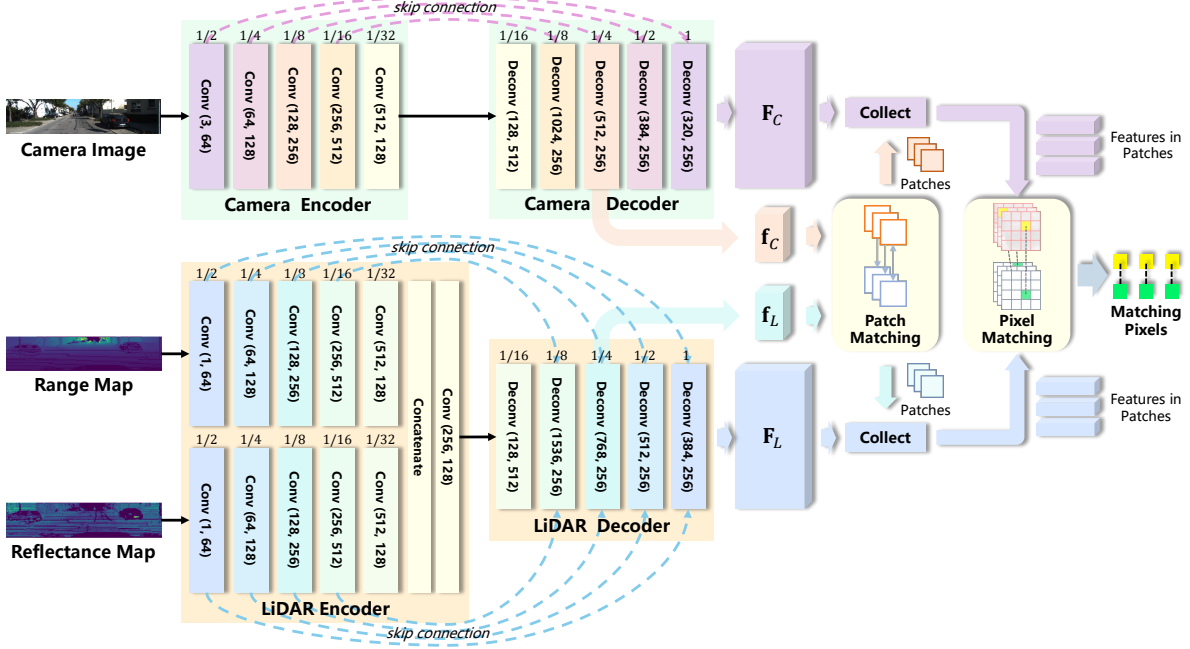


Figure 4. The overall network architecture of the proposed method, illustrates the details of the feature extraction network and the overview of the patch-to-pixel matching process. Specifically, the feature extraction network mainly consists of four parts: Camera Encoder, Camera Decoder, LiDAR Encoder, and LiDAR Decoder.

3.2. Data Pre-processing

To get a better use of the geometric characteristics of LiDAR point cloud, and mitigate the impact of domain gap between the point cloud and the image, we project the original 3D point cloud into 2D representations by a specific projection method. Currently, there are various methods for such projection, such as spherical projection [6], cylindrical projection [20], and bird’s-eye view (BEV) projection [34]. Among them, the spherical projection method can make good use of the characteristics of lateral scanning of LiDAR. However, according to the research by Wu *et al.* [34], direct spherical projection may result in numerous empty holes in the projected map, due to slight misalignments between the coordinate systems of individual lasers and the overall LiDAR system, as shown in the red area of Figure 3a. These empty areas could negatively impact subsequent registration performance.

To address this issue, we use a modified the spherical projection by associating the vertical axis of the projection map with the LaserID of the LiDAR point cloud instead of the elevation angle, which can reduce the empty holes effectively, as illustrated in Figure 3b. By using the radius in the spherical coordinate system as the information projected onto the map, we obtain the range map $\mathbf{I}_{Ra} \in \mathbb{N}^{H_R \times W_R}$. Similarly, projecting the reflectance intensity yields the reflectance map $\mathbf{I}_{Rf} \in \mathbb{N}^{H_R \times W_R}$. These maps, along with the camera image $\mathbf{I}_C \in \mathbb{N}^{H \times W \times 3}$, are fed into the sub-

sequent network. Some newer and more advanced multi-line LiDAR sensors may not experience these misalignment issues. In such cases, spherical or cylindrical projection methods can be used directly.

To explain this projection process vividly, we take the reflectance map \mathbf{I}_{Rf} as an example, as shown in Figure 3c. For an N -line LiDAR, because the horizontal axis of the projection map corresponds to the azimuth angle ϕ in the spherical coordinate system and the vertical axis corresponds to the LaserID, we can assume that we have two data points at the same azimuth angle ϕ : point A in the first line (LaserID = 0) with spherical coordinates (r_A, θ_A, ϕ) and point B in the last line (LaserID = N) with coordinates (r_B, θ_B, ϕ) , where, r_A and r_B are the spherical radii of points A and B, and θ_A and θ_B are their pitch angles. After this LaserID-based projection, they are mapped to the same column u_ϕ , with Pixel A at $(u_\phi, 0)$ in the first row and Pixel B at (u_ϕ, N) in the last row of the reflectance map.

3.3. Feature Extraction Network

Unlike other image registration tasks, the cross-modal difference between the projection map and the camera image require a specialized image feature extraction network. Additionally, to address the point cloud degradation problem within the camera’s field of view in some scenarios, we have added an extra branch for extracting reflectance features from \mathbf{I}_{Rf} alongside the spatial features from \mathbf{I}_{Ra} . This

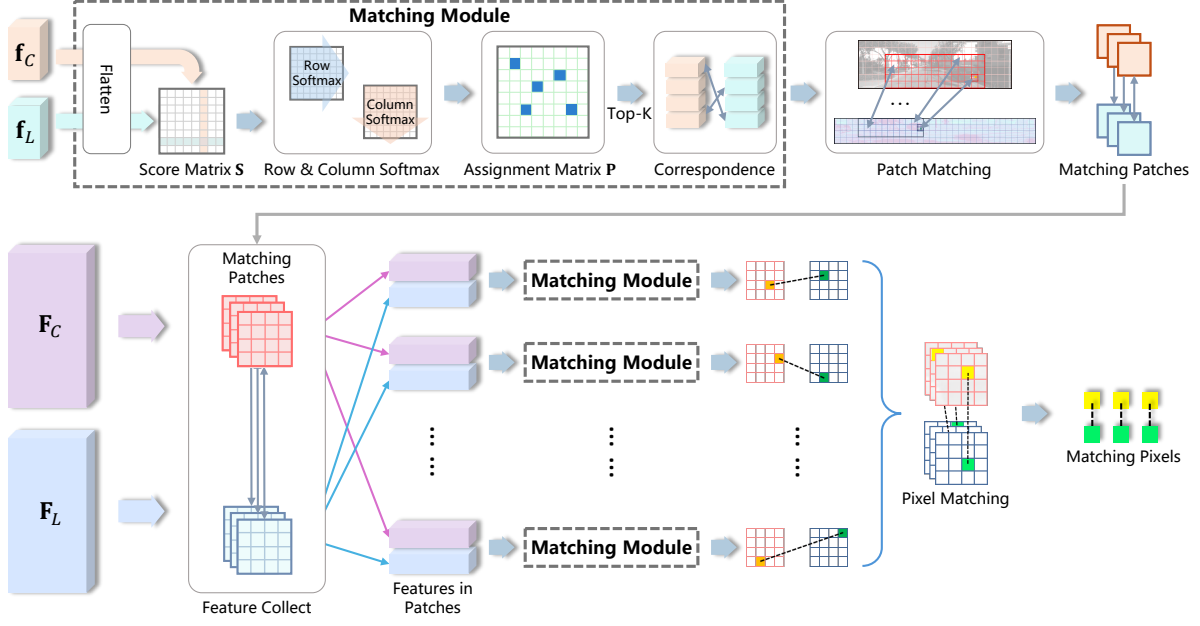


Figure 5. The detailed architecture of the patch-to-pixel matching network.

enhancement effectively increases the system’s robustness across different environments. The details of the feature extraction network architecture can be seen on the left side of Figure 4.

We employ convolutional neural networks (CNNs) to process the camera image, range map, and reflectance map. The camera encoder extracts features from \mathbf{I}_C , producing a high-dimensional feature at 1/32 of the original image scale. This small-scale, high-dimensional feature is then passed to the camera decoder. In the camera decoder network, the feature scale is gradually upsampled. First, we obtain the patch-level feature at 1/4 of the original image scale, $\mathbf{f}_C \in \mathbb{R}^{\frac{H}{4} \times \frac{W}{4} \times D_{patch}}$, where D_{patch} is the number of patch-level feature channels. Then after two layers of transposed convolution to achieve pixel-level features $\mathbf{F}_C \in \mathbb{R}^{H \times W \times D_{pixel}}$ at the original image resolution, where D_{pixel} is the number of pixel-level feature channels.

For the LiDAR encoder, which processes the projection maps, we use the same CNN architecture but with two identical encoder branches for the range map and reflectance map, respectively. The features extracted from these branches are concatenated and passed through the LiDAR decoder. The LiDAR decoder then outputs patch-level features $\mathbf{f}_L \in \mathbb{R}^{\frac{H_R}{4} \times \frac{W_R}{4} \times D_{patch}}$, and subsequently, two layers of transposed convolution are applied to obtain pixel-level features $\mathbf{F}_L \in \mathbb{R}^{H_R \times W_R \times D_{pixel}}$ at the original image scale.

3.4. Patch-to-Pixel Matching Network

To address the issue of positive sample scarcity in feature point matching caused by the limitation of the overlapping region between the camera image and the point cloud. We first conduct searches at the patch level, followed by pixel-level matching within the matched patches. This matching strategy not only solves the network supervision problem by increasing the proportion of positive samples through the patch-level searching but also significantly enhances registration accuracy through the pixel-level matching.

The structure of our matching network is shown in Figure 5. Initially, we input the patch-level features \mathbf{f}_C and \mathbf{f}_L , extracted by the feature extraction network, into a matching module to perform patch-level matching. The matching module is similar to the optimization network structure in Lightglue [18]. First, we compute the score matrix \mathbf{S} between \mathbf{f}_C and \mathbf{f}_L . Specifically, these features are flattened and then passed through a linear layer before performing matrix multiplication.

$$\mathbf{S} = \text{Linear}(\text{Flatten}(\mathbf{f}_C)) \times \text{Linear}(\text{Flatten}(\mathbf{f}_L))^T. \quad (2)$$

Next, we apply softmax operations on \mathbf{S} along both rows and columns, after computing the Hadamard product of the results we can get the soft assignment matrix \mathbf{P} ,

$$\mathbf{P}_{ij} = \frac{\exp(\mathbf{S}_{ij})}{\sum_{k=1}^{N_{2D}} \exp(\mathbf{S}_{kj})} \cdot \frac{\exp(\mathbf{S}_{ij})}{\sum_{k=1}^{N_{3D}} \exp(\mathbf{S}_{ik})}, \quad (3)$$

where \mathbf{P}_{ij} represents the value at the i -th row and j -th column of the assignment matrix \mathbf{P} , and \mathbf{S}_{ij} represents the

value at the i -th row and j -th column of the assignment matrix \mathbf{S} . We select the top- k entries from the resulting matrix to establish matches between patches based on feature similarity. Since the patch feature scale is 1/4 of the original image size, each patch corresponds to a 4×4 image region, which includes 16 pixels.

We then collect the pixel-level features from the matched patches using \mathbf{F}_C and \mathbf{F}_L , which are at the original image scale, and then we use them for pixel-level matching. This matching is done for each individual patch pair, with all pixels within each patch pair passed into another matching module, identical to the one used for patch matching, except that this module only retains the single highest similarity value (top-1). In other words, within each matching patch pair, we use the matching module to select one pair of matching pixels. By applying this process to each matching patch, we obtain the final matched pixels.

With these matched pixels, we can establish the 3D-2D correspondences between the projected 3D point cloud points and the camera image pixels. Subsequently, we use the EPnP [16] method with RANSAC [10] to solve for the pose, ultimately estimating the transformation matrix between the LiDAR point cloud and the camera image.

3.5. Loss Function

In the loss function design, we first project the LiDAR point cloud onto the camera image using the ground truth extrinsic parameters from the dataset to obtain the actual 3D-2D correspondences. Assuming we have the actual correspondences $\{C\}$, containing M correspondences, we divide each value in C by 4 and take the floor to derive the ground truth patch correspondences $\{C^*\}$. For each ground truth patch correspondence, its corresponding value in the patch matching matrix \mathbf{P} should be as large as possible. Based on this idea, we formulate the first part of our loss function, \mathcal{L}_{patch} ,

$$\mathcal{L}_{patch} = -\frac{1}{|C^*|} \sum_{(i,j) \in C^*} \log \mathbf{P}_{ij}. \quad (4)$$

During training, we do not use top- k in the matching network, instead, we use the ground truth patch correspondences for subsequent pixel-level matching directly. For each patch correspondence, the network calculates M assignment matrices \mathbf{p} . By dividing the actual correspondences C by 4 and taking the remainder, we obtain the ground truth pixel correspondences $\{\hat{C}\}$ in each \mathbf{p} matrix, which leads to the second part of our loss function, \mathcal{L}_{pixel} .

$$\mathcal{L}_{pixel} = -\frac{1}{M} \sum_{i=1}^M \log \mathbf{p}_{\hat{C}_i}^i, \quad (5)$$

where \mathbf{p}^i denotes the assignment matrix computed for the i -th pair of patches in the matching module. \hat{C}_i represents

the i -th ground truth pixel correspondence, and $\mathbf{p}_{\hat{C}_i}^i$ refers to the value at the corresponding position in \mathbf{p}^i .

During training, we supervise both parts jointly, resulting in a total loss function that is the sum of the two components, expressed as:

$$\mathcal{L}_{total} = \mathcal{L}_{patch} + \mathcal{L}_{pixel}. \quad (6)$$

4. Experimental Results and Analysis

4.1. Dataset

As in [39], we conducted experiments on the KITTI Odometry and nuScenes datasets. **KITTI Odometry**[11]. We generated image-point cloud pairs from the same data frame of 2D/3D sensors. Following previous works, we used sequences 00-08 for training and sequences 09-10 for testing. We downsample the camera image resolution to 512×160 and employ reflectance maps with a resolution of 1024×64 for both training and testing. Artificial errors applied to the point clouds during training and testing include ± 10 m two-dimensional translations along the x and y axes and arbitrary rotations around the z -axis. It is worth noting that, since the center position in the spherical coordinates of point clouds is typically fixed, translations along the x and y axes applied in other works do not accurately reflect real-world scenarios. To ensure fairness and realism, we initially applied arbitrary rotations around the z -axis to the point cloud before generating reflectance maps. then we applied translations along the x and y axes to the point cloud.

nuScenes[4]. For nuScenes, we used 850 scenes for training and 150 scenes for testing. Additionally, we downsample the camera image resolution to 320×160 and employ reflectance maps with a resolution of 1024×32 for both training and testing. Furthermore, we applied random errors ± 10 m two-dimensional translations along the x and y axes and arbitrary rotations around the z -axis to the nuScenes dataset, using the same method as KITTI.

4.2. Compared Methods

We benchmarked the proposed method against three methods: DeepI2P [17], CorrI2P [24], and VP2P-Match [39].

1. **DeepI2P**. This approach offers two distinct methods: **Grid Cls. + PnP** and **Frus. Cls. + Inv. Proj.**. The **Grid Cls. + PnP** method first segments the input image into a 32×32 grid. Then, it trains a neural network to classify 3D points into specific 2D grid cells. Finally, it uses the EPnP algorithm and RANSAC to estimate the transformation matrix \mathbf{T} . The **Frus. Cls. + Inv. Proj.** method introduces frustum classification using inverse camera projection to determine the transformation matrix, exploring both 2D and 3D inverse projections, referred to as DeepI2P(2D) and DeepI2P(3D), respectively.

Table 1. Registration accuracy on the KITTI and nuScenes datasets. Lower is better for RTE and RRE, higher is better for Acc.

Method	KITTI			nuScenes		
	RTE(m)↓	RRE(°)↓	Acc.↑	RTE(m)↓	RRE(°)↓	Acc.↑
Grid Cls. + PnP [17]	3.64 ± 3.46	19.19 ± 28.96	11.22	3.02 ± 2.40	12.66 ± 21.01	2.45
DeepI2P (3D) [17]	4.06 ± 3.54	24.73 ± 31.69	3.77	2.88 ± 2.12	20.65 ± 12.24	2.26
DeepI2P(2D) [17]	3.59 ± 3.21	11.66 ± 18.16	25.95	2.78 ± 1.99	4.80 ± 6.21	38.10
CorrI2P [24]	3.78 ± 65.16	5.89 ± 20.34	72.42	3.04 ± 60.76	3.73 ± 9.03	49.00
VP2P-Match [39]	0.75 ± 1.13	3.29 ± 7.99	83.04	0.89 ± 1.44	2.15 ± 7.03	88.33
Ours	0.21 ± 0.25	0.67 ± 0.80	99.03	0.82 ± 0.74	0.87 ± 2.12	91.50

2. **CorrI2P.** Building upon DeepI2P, CorrI2P enhances registration accuracy by using a neural network equipped with a feature exchange module and supervision of overlapping regions. This method learns correspondences between image and point cloud pairs.
3. **VP2P-Match.** VP2P-Match focuses on improving the accuracy and speed of pixel-to-point matching by leveraging sparse convolution to enhance the similarity between point cloud features and CNN-extracted image features. It incorporates a differentiable PnP solver into an end-to-end training framework, which provides a better registration performance.

4.3. Registration Accuracy

To evaluate registration accuracy and success rate, we used the same statistical methods as in VP2P-Match[39]. Specifically, we used the relative translational error (RTE) E_t and the relative rotational error (RRE) E_R to evaluate our registration results. These errors are computed as

$$E_R = \sum_{i=1}^3 |\gamma(i)|, \quad (7)$$

$$E_t = \|\mathbf{t}_{gt} - \mathbf{t}_E\|, \quad (8)$$

where $\gamma(i), i = 1, 2, 3$ are the Euler angles of the matrix $\mathbf{R}_{gt}^{-1}\mathbf{R}_E$. Here, the rotation matrix \mathbf{R}_{gt} and the translation vector \mathbf{t}_{gt} denote the transformation of the ground truth, while matrix \mathbf{R}_E and vector \mathbf{t}_E define the estimated transformation. We calculated the mean and standard deviation of all the data without removing the image-point cloud samples with large errors, as done in CorrI2P. Furthermore, for the registration success rate (Acc.), registrations with $\text{RTE} < 2m$ and $\text{RRE} < 5^\circ$ are considered successful. The final results are presented in Table 1.

At the same time, we compared the distribution of RTE and RRE in different intervals with other methods using histograms in Figure 6. We conducted the comparison on the KITTI dataset. A higher proportion in the leftward intervals indicates smaller errors. As can be seen, our method achieves around 90% of matching cases where $\text{RTE} < 0.5m$ and $\text{RRE} < 1^\circ$, significantly surpassing the other methods, which demonstrates the accuracy of the method we proposed.

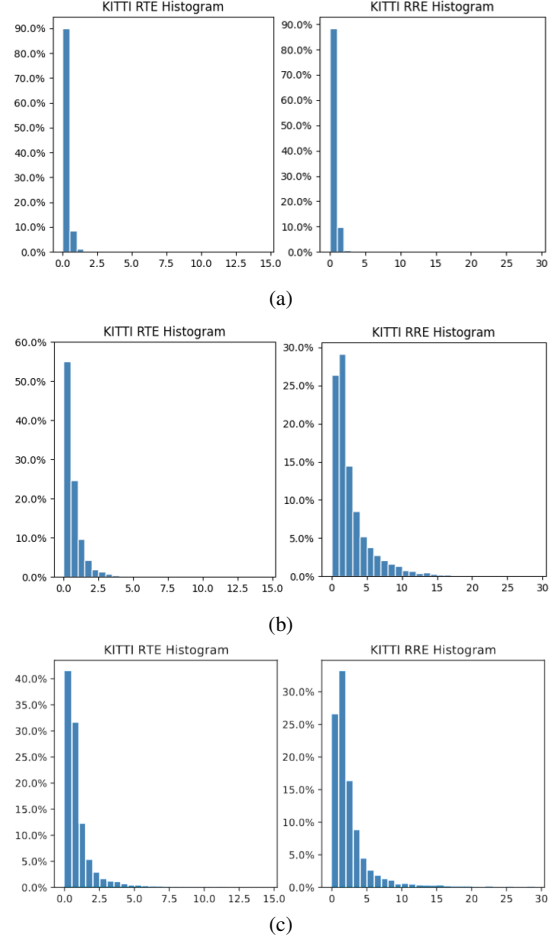


Figure 6. Histograms of distributions of RTE and RRE on the KITTI dataset. x-axis is RTE(m) and RRE(°), and y-axis is the percentage. (a) Histogram for proposed method (b) Histogram for the VP2P-Match method (c) Histogram for the CorrI2P method

4.4. Efficiency Comparison

We compared the model size and inference time of our method with other methods on a platform equipped with an NVIDIA GeForce RTX 3090 GPU and an AMD Ryzen Threadripper 2990WX. The results are shown in Table 2.

Table 2. The efficiency comparisons with other methods.

	Model Size(MB)	Inference Time(s)
DeepI2P(2D)	100.12	23.47
DeepI2P(3D)	100.12	35.61
CorrI2P	141.07	8.96
VP2P-Match	30.73	0.19
Ours	36.09	0.12

We evaluated our conducted efficiency test on the KITTI dataset, calculating the inference time per frame by dividing the total inference time with the total number of input frames. From the results of the efficiency comparison, we can see that our model has a relatively low number of parameters and short runtime, allowing the registration process to be real-time.

4.5. Visualization Result

We visualized the matching results in Figure 7. Specifically, we present the matching results between the camera image and the reflectance map. The estimated matching pixel pairs are connected by lines in this graph, which will be used for subsequent pose estimation. In the pose estimation process, outlier pairs discarded by RANSAC are marked with red lines, indicating inaccurate estimates, and the accurate matching pairs are connected by green lines. These images show that the estimated matching pairs are not only sufficiently numerous but also highly accurate. Notably, the second figure shows that even when the overlapping region of the point cloud and the image are projected onto the boundary area, we can still estimate the correspondences well, which prove the robustness of our method.

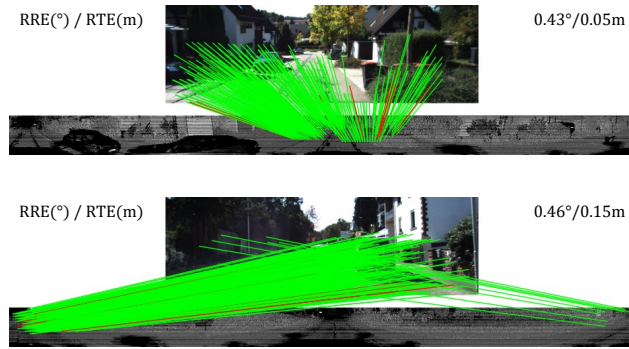


Figure 7. Visualization of the matching results. The image above is the camera image, and the one below is the reflectance map. Outlier pairs discarded by RANSAC are indicated with red lines, and accurate matching pairs are connected with green lines.

4.6. Ablation Study

In the ablation study section, we validated the effectiveness of certain network components and examined the impact of

different selections of top-k value on the network’s performance. All the experiments are conducted on the KITTI dataset.

First, we primarily conduct ablation experiments on the range map and reflectance map branches in the feature extraction network to prove the effectiveness of the additional information. The results are shown in Table 3. This table shows that neither branch achieves the best accuracy without the additional information. In some scenarios where point cloud degradation occurs within the camera’s field of view, relying solely on the range map’s point cloud geometric information fails to provide good registration. The additional reflectance information helps to address the issues in such scenes. Similarly, if only the reflectance map is used without the geometric information for assistance, it cannot handle some special cases where the reflectance information is not enough.

Second, we tested the impact of different selections of top-k value during the patch matching stage on registration accuracy and inference time, As shown in Table 4. When the top-k value is small, the accuracy slightly decreases, but the computation speed significantly improves. However, increasing the top-k value does not always lead to better performance. In fact, when the top-k value is too large, there is no significant improvement in accuracy, it results in a substantial decrease in efficiency. Therefore, in practical use, it is important to choose an appropriate value that balances both accuracy and speed.

Table 3. Experimental results on ablation of feature extraction network branches

	RTE(m)↓	RRE(°)↓	Acc.↑
reflectance only	0.29 ± 0.59	0.99 ± 3.62	98.08
range only	0.30 ± 1.23	1.08 ± 7.89	98.17
Full	0.21 ± 0.25	0.67 ± 0.80	99.03

Table 4. Results of ablation experiments on top-k selection. ‘Time’ for the inference time.

Top-k	RTE(m)↓	RRE(°)↓	Acc.↑	Time(s)↓
100	0.29 ± 0.86	0.86 ± 4.27	98.41	0.048
200	0.24 ± 0.74	0.76 ± 4.03	99.01	0.086
300	0.21 ± 0.25	0.67 ± 0.80	99.03	0.123
400	0.21 ± 0.44	0.69 ± 2.79	99.18	0.161
500	0.20 ± 0.56	0.69 ± 3.21	99.40	0.197
600	0.19 ± 0.24	0.64 ± 0.56	99.34	0.233

5. Conclusions

We propose a framework for cross-modal registration tasks by projecting 3D LiDAR point clouds into 2D representations. The projection method better leverages the geometric properties of the point clouds while reducing the impact of cross-modal differences. Furthermore, to address potential issues in the image matching process of the registration task, we introduce a multi-scale

feature extraction network and a patch-to-pixel matching strategy to get better adaption. Experiments on the KITTI and nuScenes datasets demonstrate that our network achieves exceptional accuracy, precision, and robustness.

References

- [1] Xuyang Bai, Zeyu Hu, Xinge Zhu, Qingqiu Huang, Yilun Chen, Hongbo Fu, and Chiew-Lan Tai. Transfusion: Robust lidar-camera fusion for 3d object detection with transformers. In *Proceedings of the IEEE/CVF conference on computer vision and pattern recognition*, pages 1090–1099, 2022. 1
- [2] Zixuan Bai, Guang Jiang, and Ailing Xu. Lidar-camera calibration using line correspondences. *Sensors*, 20(21):6319, 2020. 3
- [3] Eric Brachmann, Alexander Krull, Sebastian Nowozin, Jamie Shotton, Frank Michel, Stefan Gumhold, and Carsten Rother. Dsac-differentiable ransac for camera localization. In *Proceedings of the IEEE conference on computer vision and pattern recognition*, pages 6684–6692, 2017. 3
- [4] Holger Caesar, Varun Bankiti, Alex H Lang, Sourabh Vora, Venice Erin Liong, Qiang Xu, Anush Krishnan, Yu Pan, Giancarlo Baldan, and Oscar Beijbom. nuscenes: A multi-modal dataset for autonomous driving. In *Proceedings of the IEEE/CVF conference on computer vision and pattern recognition*, pages 11621–11631, 2020. 6
- [5] Luca Caltagirone, Mauro Bellone, Lennart Svensson, Matthias Wahde, and Raivo Sell. Lidar-camera semi-supervised learning for semantic segmentation. *Sensors*, 21(14):4813, 2021. 1
- [6] Xiaozhi Chen, Huimin Ma, Ji Wan, Bo Li, and Tian Xia. Multi-view 3d object detection network for autonomous driving. In *Proceedings of the IEEE conference on Computer Vision and Pattern Recognition*, pages 1907–1915, 2017. 1, 4
- [7] Christopher Choy, JunYoung Gwak, and Silvio Savarese. 4d spatio-temporal convnets: Minkowski convolutional neural networks. In *Proceedings of the IEEE/CVF conference on computer vision and pattern recognition*, pages 3075–3084, 2019. 2
- [8] Daniel DeTone, Tomasz Malisiewicz, and Andrew Rabinovich. Superpoint: Self-supervised interest point detection and description. In *Proceedings of the IEEE conference on computer vision and pattern recognition workshops*, pages 224–236, 2018. 3
- [9] Mengdan Feng, Sixing Hu, Marcelo H Ang, and Gim Hee Lee. 2d3d-matchnet: Learning to match keypoints across 2d image and 3d point cloud. In *2019 International Conference on Robotics and Automation (ICRA)*, pages 4790–4796. IEEE, 2019. 1, 3
- [10] Martin A Fischler and Robert C Bolles. Random sample consensus: a paradigm for model fitting with applications to image analysis and automated cartography. *Communications of the ACM*, 24(6):381–395, 1981. 6
- [11] Andreas Geiger, Philip Lenz, and Raquel Urtasun. Are we ready for autonomous driving? the kitti vision benchmark suite. In *2012 IEEE conference on computer vision and pattern recognition*, pages 3354–3361. IEEE, 2012. 6
- [12] Andreas Geiger, Frank Moosmann, Ömer Car, and Bernhard Schuster. Automatic camera and range sensor calibration using a single shot. In *2012 IEEE international conference on robotics and automation*, pages 3936–3943. IEEE, 2012. 3
- [13] Ganesh Iyer, R Karnik Ram, J Krishna Murthy, and K Madhava Krishna. Calibnet: Geometrically supervised extrinsic calibration using 3d spatial transformer networks. In *2018 IEEE/RSJ International Conference on Intelligent Robots and Systems (IROS)*, pages 1110–1117. IEEE, 2018. 1, 3
- [14] Eung-Su Kim and Soon-Yong Park. Extrinsic calibration of a camera-lidar multi sensor system using a planar chessboard. In *2019 Eleventh International Conference on Ubiquitous and Future Networks (ICUFN)*, pages 89–91. IEEE, 2019. 1, 3
- [15] Jason Ku, Melissa Mozifian, Jungwook Lee, Ali Harakeh, and Steven L Waslander. Joint 3d proposal generation and object detection from view aggregation. In *2018 IEEE/RSJ International Conference on Intelligent Robots and Systems (IROS)*, pages 1–8. IEEE, 2018. 1
- [16] Vincent Lepetit, Francesc Moreno-Noguer, and Pascal Fua. Ep n p: An accurate o (n) solution to the p n p problem. *International journal of computer vision*, 81:155–166, 2009. 3, 6
- [17] Jiaxin Li and Gim Hee Lee. Deepi2p: Image-to-point cloud registration via deep classification. In *Proceedings of the IEEE/CVF Conference on Computer Vision and Pattern Recognition*, pages 15960–15969, 2021. 3, 6, 7
- [18] Philipp Lindenberger, Paul-Edouard Sarlin, and Marc Pollefeys. Lightglue: Local feature matching at light speed. In *Proceedings of the IEEE/CVF International Conference on Computer Vision*, pages 17627–17638, 2023. 5
- [19] Xudong Lv, Boya Wang, Ziwen Dou, Dong Ye, and Shuo Wang. Lccnet: Lidar and camera self-calibration using cost volume network. In *Proceedings of the IEEE/CVF Conference on Computer Vision and Pattern Recognition*, pages 2894–2901, 2021. 3
- [20] Andres Milioto, Ignacio Vizzo, Jens Behley, and Cyrill Stachniss. Rangenet++: Fast and accurate lidar semantic segmentation. In *2019 IEEE/RSJ international conference on intelligent robots and systems (IROS)*, pages 4213–4220. IEEE, 2019. 4
- [21] Quang-Hieu Pham, Mikaela Angelina Uy, Binh-Son Hua, Duc Thanh Nguyen, Gemma Roig, and Sai-Kit Yeung. Lcd: Learned cross-domain descriptors for 2d-3d matching. In *Proceedings of the AAAI conference on artificial intelligence*, pages 11856–11864, 2020. 1, 3
- [22] Charles Ruizhongtai Qi, Li Yi, Hao Su, and Leonidas J Guibas. Pointnet++: Deep hierarchical feature learning on point sets in a metric space. *Advances in neural information processing systems*, 30, 2017. 3
- [23] Charles Ruizhongtai Qi, Li Yi, Hao Su, and Leonidas J Guibas. Pointnet++: Deep hierarchical feature learning on point sets in a metric space. *Advances in neural information processing systems*, 30, 2017. 2
- [24] Siyu Ren, Yiming Zeng, Junhui Hou, and Xiaodong Chen. Corri2p: Deep image-to-point cloud registration via dense

- correspondence. *IEEE Transactions on Circuits and Systems for Video Technology*, 33(3):1198–1208, 2022. [1](#), [3](#), [6](#), [7](#)
- [25] Paul-Edouard Sarlin, Cesar Cadena, Roland Siegwart, and Marcin Dymczyk. From coarse to fine: Robust hierarchical localization at large scale. In *Proceedings of the IEEE/CVF conference on computer vision and pattern recognition*, pages 12716–12725, 2019. [3](#)
- [26] Paul-Edouard Sarlin, Daniel DeTone, Tomasz Malisiewicz, and Andrew Rabinovich. Superglue: Learning feature matching with graph neural networks. In *Proceedings of the IEEE/CVF conference on computer vision and pattern recognition*, pages 4938–4947, 2020. [3](#)
- [27] Nick Schneider, Florian Piewak, Christoph Stiller, and Uwe Franke. Regnet: Multimodal sensor registration using deep neural networks. In *2017 IEEE intelligent vehicles symposium (IV)*, pages 1803–1810. IEEE, 2017. [1](#)
- [28] Yi Sun, Jian Li, Yuru Wang, Xin Xu, Xiaohui Yang, and Zhenping Sun. Atop: An attention-to-optimization approach for automatic lidar-camera calibration via cross-modal object matching. *IEEE Transactions on Intelligent Vehicles*, 8(1): 696–708, 2022. [3](#)
- [29] Mihkel Väli and Juhan-Peep Ernits. *Evaluation of multiple lidar placement on a self-driving car in Autoware*. PhD thesis, Tallinn University of Technology Tallinn, Estonia, 2018. [3](#)
- [30] Bing Wang, Changhao Chen, Zhaopeng Cui, Jie Qin, Chris Xiaoxuan Lu, Zhengdi Yu, Peijun Zhao, Zhen Dong, Fan Zhu, Niki Trigoni, et al. P2-net: Joint description and detection of local features for pixel and point matching. In *Proceedings of the IEEE/CVF International Conference on Computer Vision*, pages 16004–16013, 2021. [3](#)
- [31] Weiyue Wang and Ulrich Neumann. Depth-aware cnn for rgb-d segmentation. In *Proceedings of the European conference on computer vision (ECCV)*, pages 135–150, 2018. [1](#)
- [32] Weimin Wang, Shohei Nobuhara, Ryosuke Nakamura, and Ken Sakurada. Soic: Semantic online initialization and calibration for lidar and camera. *arXiv preprint arXiv:2003.04260*, 2020. [3](#)
- [33] Bichen Wu, Alvin Wan, Xiangyu Yue, and Kurt Keutzer. Squeezeseg: Convolutional neural nets with recurrent crf for real-time road-object segmentation from 3d lidar point cloud. In *2018 IEEE international conference on robotics and automation (ICRA)*, pages 1887–1893. IEEE, 2018. [1](#)
- [34] Tao Wu, Hao Fu, Bokai Liu, Hanzhang Xue, Ruike Ren, and Zhiming Tu. Detailed analysis on generating the range image for lidar point cloud processing. *Electronics*, 10(11):1224, 2021. [4](#)
- [35] Chao Ye, Huihui Pan, and Huijun Gao. Keypoint-based lidar-camera online calibration with robust geometric network. *IEEE Transactions on Instrumentation and Measurement*, 71:1–11, 2021. [3](#)
- [36] Kaiwen Yuan, Zhenyu Guo, and Z Jane Wang. Rgnet: Tolerance aware lidar-camera online calibration with geometric deep learning and generative model. *IEEE Robotics and Automation Letters*, 5(4):6956–6963, 2020. [1](#), [3](#)
- [37] Mohammad Ali Zaiter, Régis Lherbier, Ghaleb Faour, Oussama Bazzi, and Jean-Charles Noyer. Extrinsic lidar/ground calibration method using 3d geometrical plane-based estimation. *Sensors*, 20(10):2841, 2020. [3](#)
- [38] Qilong Zhang and Robert Pless. Extrinsic calibration of a camera and laser range finder (improves camera calibration). In *2004 IEEE/RSJ International Conference on Intelligent Robots and Systems (IROS)(IEEE Cat. No. 04CH37566)*, pages 2301–2306. IEEE, 2004. [3](#)
- [39] Junsheng Zhou, Baorui Ma, Wenyuan Zhang, Yi Fang, Yu-Shen Liu, and Zhizhong Han. Differentiable registration of images and lidar point clouds with voxelpoint-to-pixel matching. *Advances in Neural Information Processing Systems*, 36, 2024. [2](#), [3](#), [6](#), [7](#)
- [40] Lipu Zhou, Zimo Li, and Michael Kaess. Automatic extrinsic calibration of a camera and a 3d lidar using line and plane correspondences. In *2018 IEEE/RSJ International Conference on Intelligent Robots and Systems (IROS)*, pages 5562–5569. IEEE, 2018. [3](#)
- [41] Qunjie Zhou, Sérgio Agostinho, Aljoša Ošep, and Laura Leal-Taixé. Is geometry enough for matching in visual localization? In *European Conference on Computer Vision*, pages 407–425. Springer, 2022. [3](#)
- [42] Yufeng Zhu, Chenghui Li, and Yubo Zhang. Online camera-lidar calibration with sensor semantic information. In *2020 IEEE International Conference on Robotics and Automation (ICRA)*, pages 4970–4976. IEEE, 2020. [3](#)